Chemical Science

ROYAL SOCIETY OF CHEMISTRY

EDGE ARTICLE

View Article Online
View Journal | View Issue

Cite this: *Chem. Sci.*, 2024, **15**, 11488

All publication charges for this article have been paid for by the Royal Society of Chemistry

A robust Fe-based heterogeneous photocatalyst for the visible-light-mediated selective reduction of an impure CO_2 stream†

Topi Ghosh,‡[a] Peng Ren, ‡[ab] Philippe Franck,[a] Min Tang,[c] Aleksander Jaworski, [d] Giovanni Barcaro,[e] Susanna Monti, [f] Lata Chouhan,[g] Jabor Rabeah, [h] Alina Skorynina,[i] Joaquin Silvestre-Albero, [j] Laura Simonelli, [i] Anna Rokicińska, [k] Elke Debroye,[g] Piotr Kuśtrowski, [k] Sara Bals [c] and Shoubhik Das *[ab]

Received 26th April 2024
Accepted 7th June 2024

DOI: 10.1039/d4sc02773f

rsc.li/chemical-science

The transformation of CO_2 into value-added products from an impure CO_2 stream, such as flue gas or exhaust gas, directly contributes to the principle of carbon capture and utilization (CCU). Thus, we have developed a robust iron-based heterogeneous photocatalyst that can convert the exhaust gas from the car into CO with an exceptional production rate of 145 μmol g^{-1} h^{-1}. We characterized this photocatalyst by PXRD, XPS, ssNMR, EXAFS, XANES, HR-TEM, and further provided mechanistic experiments, and multi-scale/level computational studies. We have reached a clear understanding of its properties and performance that indicates that this highly robust photocatalyst could be used to design an efficient visible-light-mediated reduction strategy for the transformation of impure CO_2 streams into value-added products.

Introduction

The development of iron-based catalysts is attractive due to the high abundance of iron in the Earth's crust and low cost compared to the other transition metals.[1–8] Furthermore, iron can adopt diverse oxidation states (from −2 to +5) and can promote single electron transfer reactions.[9] These advantages triggered scientists to develop novel iron-based homo-/heterogeneous catalysts, and many of them are comparable to those of the 4d and 5d-based transition metal analogs.[10–13] Parallel to the development of iron-based catalysts, the direct transformation of CO_2 into value-added products has tremendous potential because CO_2 is non-toxic and abundant in the atmosphere.[14–27] However, in most cases, only pure CO_2 streams are used as carbon sources. If impure CO_2 streams such as flue gas from industries or exhaust gas from a car could be utilized, it will avoid the associated cost and energy requirement for the

[a]*Department of Chemistry, University of Antwerp, Antwerp, Belgium. E-mail: Shoubhik.Das@uni-bayreuth.de*

[b]*Department of Chemistry, University of Bayreuth, Bayreuth, Germany*

[c]*EMAT and NANO Lab Center of Excellence, Department of Physics, University of Antwerp, Antwerp, Belgium*

[d]*Department of Materials and Environmental Chemistry, Stockholm University, Stockholm, Sweden*

[e]*CNR-IPCF, Institute for Chemical and Physical Processes, via G. Moruzzi 1, 56124 Pisa, Italy*

[f]*CNR-ICCOM, Institute of Chemistry of Organometallic Compounds, via G. Moruzzi 1, 56124 Pisa, Italy*

[g]*Department of Chemistry, KU Leuven, Leuven, Belgium*

[h]*Leibniz-Institut für Katalyse e. V, Albert-Einstein-Straße 29a, 18059 Rostock, Germany*

[i]*CLAESS Beamline, ALBA Synchroton, Spain*

[j]*Departamento de Quimica Inorganica-Instituto Universitario de Materiales, Universidad de Alicante, Alicante E-03080, Spain*

[k]*Faculty of Chemistry, Jagiellonian University, Krakow, Poland*

† Electronic supplementary information (ESI) available. See DOI: https://doi.org/10.1039/d4sc02773f

‡ Denotes equal contributions.

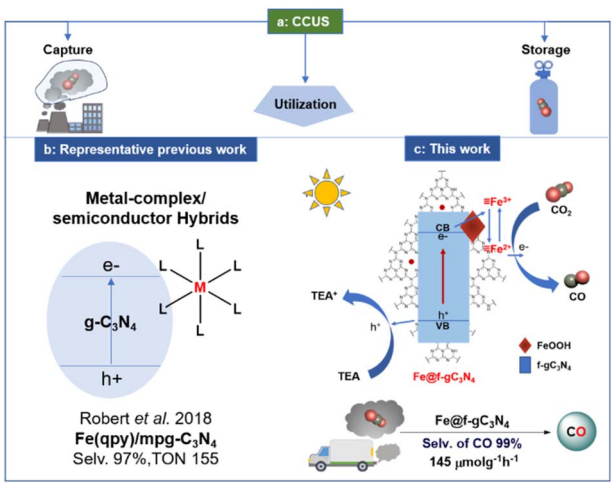

Scheme 1 Reported photocatalytic approaches and our work for the reduction of carbon dioxide.

CO_2 purification procedure. This new approach contributes to the Carbon Capture and Utilization (CCU) principle (Scheme 1a).[28–39] Nonetheless, the presence of impurities such as O_2, water vapor, CO, NO_x, and hydrocarbons in the impure CO_2 stream can be harmful to the photocatalyst and can be detrimental to the desired product formation.[40–44]

Recently, graphitic carbon nitrides (g-C_3N_4) have become highly attractive as photocatalysts due to their high chemical and thermal stability, appropriate band structures, and low cost.[45–51] Thus, researchers have employed g–C_3N_4–based hybrid photocatalysts (g-C_3N_4 combined with Ru,[52] Co,[53–56] and Fe[57–59]-based metal complexes) to improve the selectivity and reactivity for the reduction of CO_2 into CO (Scheme 1b). Among them, Co-based transition metal complexes such as $[Co(bpy)_3]^{2+}$ and Co(qpy) along with g-C_3N_4, exhibited the selectivity of 86 and 98% (TON of CO were 3.7 and 128, with the production rate of 37 and 7.98 μmol g^{-1} h^{-1} respectively) for the formation of CO in the presence of triethanolamine (TEOA) and 1,3-dimethyl-2-phenyl-2,3-dihydro-1*H*-benzo[*d*]imidazole (BIH) as sacrificial reductant.[54,56] Additionally, Fe-based metal complexes such as $Fe(qpy)_3$ and Fe(qpy)-BA exhibited the formation of CO with a production rate of 91 and 141 μmol g^{-1} h^{-1} respectively (selectivity was 97 and 95% in the presence of TEOA and TEA + BIH as sacrificial reductant).[57,58] However, these hybrid systems always required expensive ligands and multistep synthetic routes (associated with the metal complexes), exhibited poor recyclability, and rarely showed reactivity toward the transformation of an impure CO_2 stream.

To achieve a robust and recyclable Fe-based photocatalyst, construction of composite material could be a promising route since this could address the rapid recombination of photogenerated carriers which are the common limitations for the photocatalytic reactivity of g-C_3N_4.[60,61] Along this direction, amorphous iron-based oxyhydroxides (FeOOH), known as promising Fenton-like catalysts, should be ideal for hybridization due to their small particle size.[62–64] The coupling of amorphous FeOOH with g-C_3N_4 could be a sound strategy for constructing an effective recyclable photocatalyst. Considering this, we first modified the g-C_3N_4 moiety by introducing an aryl functionality (f-gC_3N_4) to improve the photocatalytic properties of g-C_3N_4 (ref. 49) and later, FeOOH was introduced into the moiety to fabricate a FeOOH/f-gC_3N_4 composite photocatalyst. This photocatalyst generated CO with a production rate of 304 μmol g^{-1} h^{-1} with a selectivity of 99%. Expediently, when exhaust gas from a car was applied, CO was formed with a production rate of 145 μmol g^{-1} h^{-1} (Scheme 1c), thanks to the enhanced interfacial electron transfer between FeOOH and f-gC_3N_4. To the best of our knowledge, this is the first Fe-based recyclable photocatalytic system that can be applied for the reduction of impure CO_2 stream.

Results and discussion

At the beginning of this project, g-C_3N_4 was synthesized by calcinating dicyandiamide (DCDA) at 550 °C for 4 h (temp. increasing rate = 2.2 °C min^{-1}) in a tube furnace under aerobic conditions (please see the detailed procedure in the ESI†).[49] Followed by this method, functionalized graphitic carbon nitrides (f-gC_3N_4) were achieved by stirring a mixture of 9 gm of DCDA and 150 mg of 2-amino-5-trifluoromethyl benzonitrile in deionized water (45 mL) at 95 °C until it's completely dried, resulting mixture was then grinded in an algae mortar and was calcined at 550 °C for 4 h (temp. increasing rate = 2.2 °C min^{-1}) under aerobic conditions (please see in the ESI†). Later, $Fe(NO_3)_3 \cdot 9H_2O$ (7.23 mg for 0.2Fe@f-gC_3N_4, 18 mg for 0.5Fe@f-gC_3N_4, 25.3 mg for 0.7Fe@f-gC_3N_4, and 36 mg for 1Fe@f-gC_3N_4) and f-gC_3N_4 (500 mg) were mixed in 10 mL deionized water and the reaction mixture was further stirred at 100 °C (please see in the ESI† for the detailed procedure). It should be noted that 0.2Fe@f-gC_3N_4, 0.5Fe@f-gC_3N_4, 0.7Fe@f-gC_3N_4 and 1Fe@f-gC_3N_4 denotes 0.2, 0.5, 0.7 and 1 wt% of iron loading on f-gC_3N_4 respectively. After the synthesis of all these photocatalysts, the Tauc plot exhibited that gC_3N_4, f-gC_3N_4, 0.5Fe@g-C_3N_4, 1Fe@f-gC_3N_4, 0.7Fe@f-gC_3N_4, 0.5Fe@f-gC_3N_4, and 0.2Fe@f-gC_3N_4 had the band gap of 2.64, 2.48, 2.46, 2.34, 2.47, 2.46 and 2.46 eV, respectively (Fig. S3†). Furthermore, Mott–Schottky plots of all these photocatalysts disclosed that the flat band (fb) potential of gC_3N_4, f-gC_3N_4, 0.5Fe@g-C_3N_4, 1Fe@f-gC_3N_4, 0.7Fe@f-gC_3N_4, 0.5Fe@f-gC_3N_4, and 0.2Fe@f-gC_3N_4 were −0.34, −0.44, −0.47, −0.52, −0.56, −0.33 and −0.38 eV *vs.* Normal Hydrogen Electrode (NHE). Additionally, the positive slope indicated the n-type nature of these semiconductors (Fig. S4†). The conduction band (CB) of an n-type inorganic semiconductor is commonly assumed to be ≈ −0.2 V negative than the flat band potentials. Thus, the CB potentials were derived by lowering the flat band potential by 0.2 V compared to the NHE (Fig. S5†).[47,65]

After the synthesis, photocatalytic experiments were carried out in 4 mL of CO_2-saturated acetonitrile solution in the presence of a freshly distilled sacrificial electron donor (ACN : triethylamine, 4 : 1 V/V), under the irradiation of a Kessil lamp for 18 h (λ = 427 nm, 100 mW cm^{-2} light intensity, Table S1†). Indeed, CO was the primary product, with a minor quantity of CH_4 and H_2 In this photocatalytic reaction, TEA got oxidized to form $TEAH^+$.[58] To our observation, only a trace amount of CO and H_2 were obtained in the case of g-C_3N_4, while a moderate amount of CO with 91% selectivity was observed in the presence f-gC_3N_4. Furthermore, when 0.5 wt% of Fe was deposited onto both gC_3N_4 and f-gC_3N_4, the Fe@f-gC_3N_4 system exhibited nearly 12 times higher production rate of CO. To investigate the superior role of 0.5 wt% Fe@f-gC_3N_4 photocatalyst, pure $Fe(NO_3)_3 \cdot 9H_2O$ was mixed externally with f-gC_3N_4 (iron content was the same as 0.5Fe@f-gC_3N_4). A lower quantity of CO clearly confirmed the importance of the deposition of iron onto f-gC_3N_4 structure. It could be due to the fact that the metal deposition enhanced the charge transfer efficiency from the conduction band of f-gC_3N_4 to the active metal site of Fe^{+n} and that was ideal for the effective reduction of CO_2.[57] After that, we were able to further increase the catalytic reactivity through different loadings of iron (0.2–1 wt%) on f-gC_3N_4 (Fig. 1a and b). We observed that the production rate of CO was linearly increased up to 0.7 wt% and was drastically boosted for 1Fe@f-gC_3N_4 (172 μmol g^{-1} h^{-1}). Indeed, iron sites are prone to adsorb CO_2; therefore, with the increase of iron loadings, more electrons will be transferred to the iron sites to reduce CO_2. Thus,

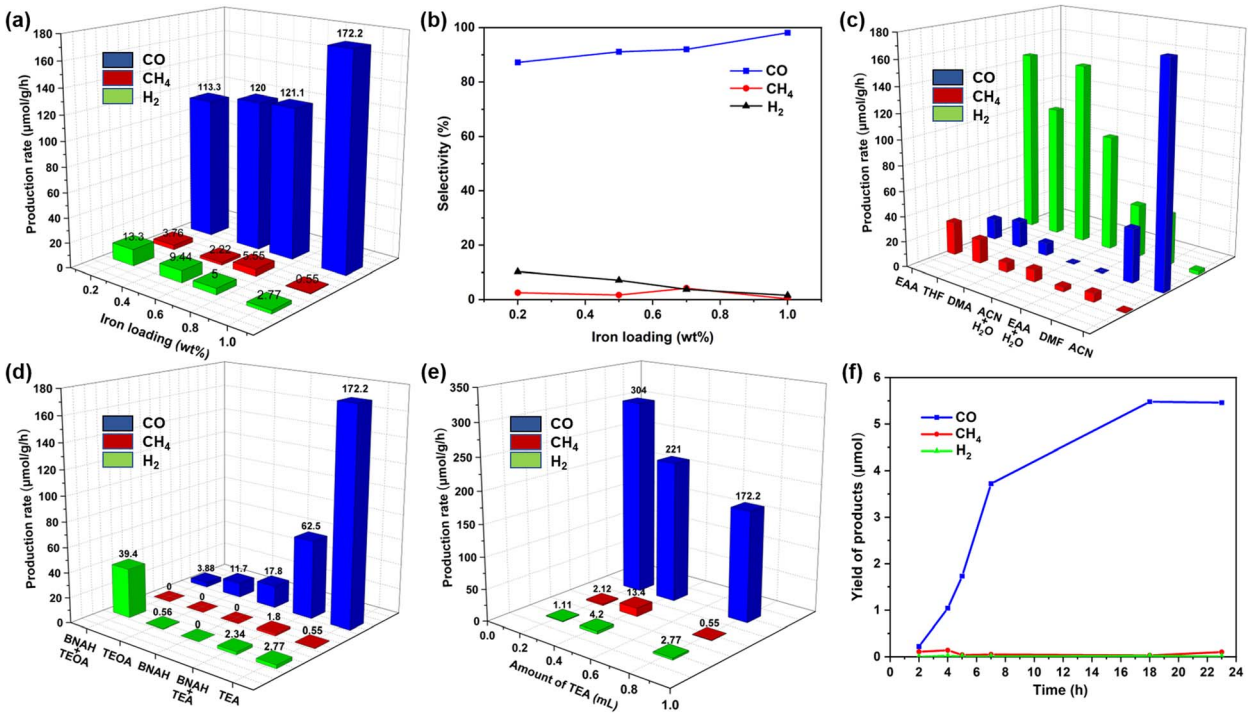

Fig. 1 (a) Reduction of CO_2 by using different loading of iron catalysts; (b) selectivity in CO_2 reduced products by using different loading of iron catalysts; (a and b) reaction conditions: iron catalyst (1 mg), TEA (0.8 mL), ACN (3.2 mL), time = 18 h, λ = 427 nm, reaction temperature = 30 °C. (c) Photocatalytic CO_2 reduction by using different solvents. Reaction conditions: 1Fe@f-gC_3N_4 (1 mg), TEA (0.8 mL), different solvents (3.2 mL), time = 18 h, λ = 427 nm, reaction temperature = 30 °C. (d) Photocatalytic reduction of CO_2 by using different reductants. Reaction conditions: 1Fe@f-gC_3N_4 (1 mg), different reductant for single reductant system TEA or TEOA (0.8 mL), 0.1 M BNAH, for binary reductant system BNAH (32 mg) + TEOA (0.4 mL), BNAH (32 mg) + TEA (0.4 mL), ACN (3.2 mL), time = 18 h, λ = 427 nm, reaction temperature = 30° (e) production rate of photocatalytic CO_2 reduction by using different amount of TEA. Reaction conditions: catalyst 1Fe@f-gC_3N_4 (1 mg), TEA (0.2, 0.4, 0.8 mL), solvent ACN (3.2–3.8 mL), time = 18 h, λ = 427 nm, reaction temperature = 30 °C. (f) Kinetic studies for the photocatalytic reduction of pure CO_2. Reaction conditions: 1Fe@f-gC_3N_4 (1 mg), TEA (0.2 mL), ACN (3.8 mL), time = 2–23 h, λ = 427 nm, reaction temperature = 30 °C.

the increased Fe-loading prolonged the lifetime of the charge carriers and enhanced the transfer of the photogenerated electrons from f-gC_3N_4 to the Fe^{+n} center and then to CO_2. Instead, a smaller number of electrons were transferred toward proton reduction, which in turn suppressed H_2 evolution,[67] and the production rate and selectivity to CO were linearly increased with the increase of iron loading.

Then, we evaluated the importance of different solvents (CH_3CN, DMF, DMA, EtOAc, THF and H_2O) in the presence of 1Fe@f-gC_3N_4 (Fig. 1c). While all of them were favorable for this transformation, no reaction took place in pure water, and further addition of water to organic solvents such as CH_3CN and EtOAc resulted in a lower evolution rate of CO. Surprisingly, in the aqueous binary solvent system, CH_4 and H_2 were the major products, and CO was the minor product (Fig. 1c). In fact, by adding 37% of water into CH_3CN and EtOAc, the selectivity of the CO_2 reduction product was changed entirely from CO to CH_4 ($8e^-/8H^+$ reduction process) with a production rate of 9.30 and 3.53 μmol g^{-1} h^{-1} respectively. This could be attributed to the fact that the addition of water increased the number of available protons in the solution, which in turn took part in the CO_2 reduction process to form CH_4.[68] Nevertheless, among all the solvents, CH_3CN was the best for the photochemical reduction of CO_2 to CO, with a high production rate of 172.2 μmol g^{-1} h^{-1} and an excellent selectivity of 98%. Additionally, sacrificial reductants such as triethylamine (TEA), triethanolamine (TEOA) and 1-benzyl-1,4-dihydronicotinamide (BNAH) were also investigated and a production rate of 172, 11.7, and 17.8 μmol g^{-1} h^{-1} with 98, 95, and 100% selectivity were obtained (Fig. 1d). Further investigations by using different amounts of TEA and reducing the amount of TEA to 0.2 mL resulted in an excellent production rate of 304 μmol g^{-1} h^{-1} (Fig. 1e). We argued that a higher concentration of TEA probably quenched the excited state of the photocatalyst and decreased the photocatalytic efficiency.[69]

Furthermore, control experiments suggested that in the absence of CO_2, photocatalyst, and light, no formation of CO was observed (Fig. S8†). On the other hand, in the absence of TEA, the formation of CO was observed, but with a lower production rate of 76.6 μmol g^{-1} h^{-1}. In these conditions, the kinetics of CO_2 reduction exhibited a linear increase in CO production up to 18 h, and after this, the yield of CO remained constant but the production of CH_4 was slightly increased. Furthermore, kinetic studies demonstrated that the evolution of CO was stable up to 23 h, which was comparable with the recently reported photocatalysts (Fig. 1f).[57,70]

To demonstrate the application of this chemistry, the exhaust gas (containing impurities besides CO_2, are shown in

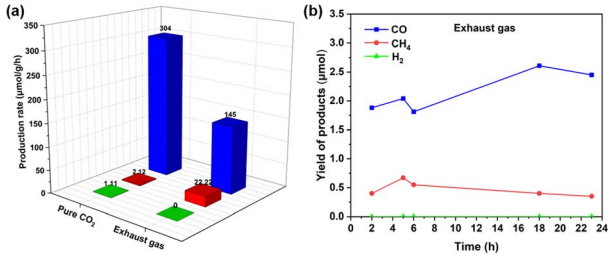

Fig. 2 (a) Comparison of photocatalytic CO_2 reduction by using pure CO_2 and by using exhaust gas. Reaction conditions: 1Fe@f-gC_3N_4 (1 mg), TEA (0.2 mL), ACN (3.8 mL), time = 18 h, λ = 427 nm, reaction temp. = 30 °C. (b) Kinetic studies for the photocatalytic reduction of exhaust gas. Reaction conditions: 1Fe@f-gC_3N_4 (1 mg), TEA (0.2 mL), ACN (3.8 mL), λ = 427 nm, reaction temp. = 30 °C.

Fig. S7†) was directly collected from a vehicle by using gas sampling bags (Fig. S6†) and was applied directly under these reaction conditions, showing a CO production rate of 145 μmol g^{-1} h^{-1} (Fig. 2a). This decreased catalytic reactivity was due to the combined result of lower CO_2 concentration in the exhaust gas as well as the presence of NO_x or SO_x in the exhaust gas, which can also be adsorbed on the active catalytic sites.[71] In addition, the kinetic studies demonstrated the high stability of this photocatalyst in the presence of impurities such as H_2, CO, CH_4, O_2, N_2, and others, which are typically present in car exhaust gas (Fig. 2b). Furthermore, to estimate the reusability of this photocatalyst, 10 mg of the material was successfully used (under the same reaction conditions) and recycled for up to three cycles (Fig. S10†).

To achieve a deep characterization of the synthesized materials, we investigated the morphology and the structure of 1Fe@f-gC_3N_4 by High-Angle Annular Dark Field Scanning Transmission Electron Microscopy (HAADF-STEM). As shown in Fig. 3a, nanoparticles (NPs) were non-uniformly distributed over f-gC_3N_4, and EDX-mapping demonstrated that the NPs contained Fe (Fig. 3b–e). Atomic resolution HAADF-STEM images were acquired at lower (Fig. 3f) and higher (Fig. 3g) magnification. Fast Fourier transform (FFT) of the NPs marked by the red dashed rectangle in Fig. 3g provided lattice spacings of 2.690 Å, 2.580 Å, and 2.446 Å (Fig. 3h), which corresponded to FeO(OH) (130), (0−21), and (111), respectively. These results demonstrated that the supported NPs correspond to FeO(OH) species, and further investigating the edge of the f-gC_3N_4 support, bright dots marked by yellow dashed circles were observed, corresponding to small clusters containing Fe (Fig. 3i).

The crystal structure of prepared gC_3N_4, f-gC_3N_4, and 1Fe@f-gC_3N_4 were further investigated *via* XRD. Two distinct diffraction peaks were observed at 12.9° and 27.3°, corresponding to the (100) and (002) crystal planes of g-C_3N_4, related to the in-plane repeating *s*-triazine structural moieties and interlayer stacking of the conjugated aromatic ring (Fig. S11†).[72–74] While for f-gC_3N_4, the peak position and the peak intensity were almost similar with gC_3N_4, in the presence of Fe, the intensity of diffraction peak (002 in case of 1Fe@f-gC_3N_4) was slightly decreased as well as a marginal shift to higher diffraction angle

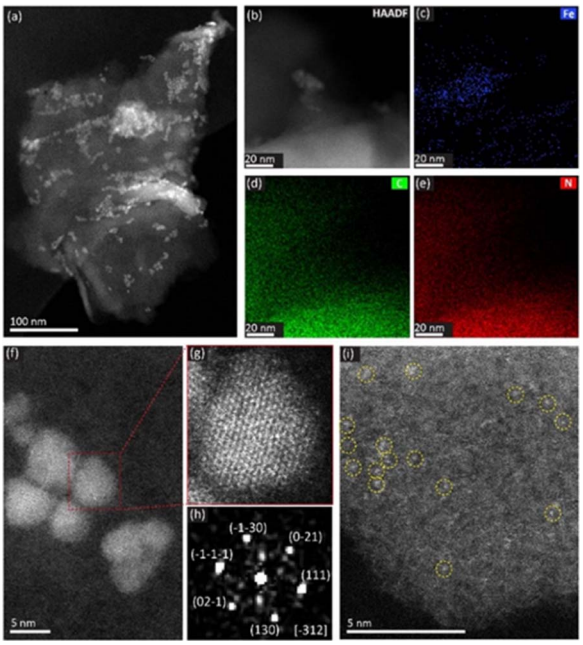

Fig. 3 (a) HAADF-STEM image showing the morphology of 1Fe@f-gC_3N_4. (b–e) HAADF-STEM image (b) and EDX mapping results (c–e) showing the support f-gC_3N_4 and the Fe nanoparticles. (f) Atomic resolution HAADF-STEM image showing the Fe_2O_3 nanoparticles. (g) Image of magnified area in f marked by red dashed rectangles. (h) Fast Fourier transform (FFT) pattern of the FeO(OH) nanoparticles in 1Fe@f-gC_3N_4 (g). The direction is FeO(OH) [−312]. (i) Atomic resolution image showing the Fe clusters.

was observed.[73,75] However, no obvious diffraction peak of Fe_2O_3 or FeO(OH) phase were detected in the pattern of 1Fe@f-gC_3N_4, due to relatively low amount of the Fe species.[66,76,77] Additionally, the weakening of the intensity of (002) peak suggested a decrease in crystallinity, with a consequent increase in the number of defects. These could trap a large number of carriers, with a resulting increase in charge separation and an improvement of the photocatalytic performance.[75]

To verify the atomic environment of Fe in 1Fe@f-gC_3N_4, synchrotron X-ray absorption near-edge structure (XANES) and extended X-ray absorption fine structure (EXAFS) at Fe K-edge were performed and compared to the X-ray absorption spectra of the Fe_2O_3 and FeOOH reference materials. From the position of the rising edge in XANES spectra (Fig. 4a), it can be concluded that Fe in 1Fe@f-gC_3N_4 was predominantly in a +3 oxidation state, as confirmed by the close resemblance with Fe_2O_3 and FeOOH pre-edge peaks. EXAFS and Fourier transformed (FT) k^3-weighted EXAFS curves were further extracted to probe the atomic iron-based local structures (Fig. 4b and c). When compared with the reference systems, 1Fe@f-gC_3N_4 nearly matched the peaks of FeOOH, which was especially noticeable for the shell scattering peaks of the longer-range order (2–3.5 Å), indicating Fe–Fe bonding. Concurrently, only FeOOH species could not fully describe XANES region and first shell, and a low Fe_2O_3 fraction below 5% cannot be excluded.

Solid-state MAS NMR spectra of all NMR-active nuclei present in the material (^{1}H, ^{13}C, ^{15}N, and ^{19}F) were also collected

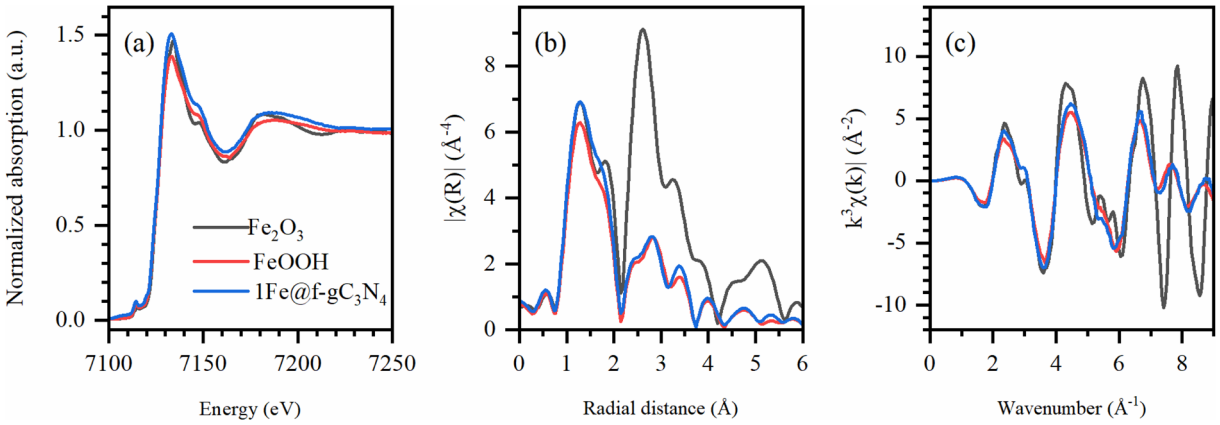

Fig. 4 (a) Normalized XANES spectra, (b) FT-EXAFS spectra (phase uncorrected) and (c) k^3-weighted EXAFS spectra at Fe K-edge for the 1Fe@f-gC_3N_4 and reference samples (Fe_2O_3 and FeOOH).

to probe the local structure and to examine potential structural changes upon doping of the f-gC_3N_4 with Fe^{n+} species (Fig. S12†). The ^{1}H MAS, ^{13}C CPMAS, and ^{15}N CPMAS spectra were almost identical to NMR data we collected from the related polymeric carbon nitride catalysts and reported recently.[49,78] Therefore, we concluded that the overall structure and polymerization degree in these materials were not affected to any significant extent by doping with Fe^{n+} ions. However, in the ^{19}F MAS NMR spectrum, the ^{19}F NMR shift of −120 ppm was distinct from that of −105 ppm observed by us for the undoped f-gC_3N_4, attributed to the presence of $=CF_2$ groups (Fig. S12b†).[49,79,80] Moreover, an additional weak signal at −202 ppm was detected, which had not been observed for the undoped material. The additional ^{19}F MAS spectrum recorded using a short 0.2 s relaxation delay was collected to inspect if the appearance of the signal at −202 ppm could be related to the introduction of Fe^{n+} ions in the material. Upon using a short relaxation delay of 0.2 s, the intensity of the signal at −202 ppm was almost unaffected, whereas the signal at −120 ppm was significantly saturated. This could be attributed to the paramagnetic relaxation enhancement of the ^{19}F nuclei in close contact with paramagnetic Fe^{n+} ions. The observed ^{19}F NMR shifts of −120 and −202 ppm were most probably affected by the induced paramagnetic NMR shift interactions.[81]

The XPS spectra were recorded in the Fe 2p, C 1s, and N 1s regions for both fresh and used samples of 1Fe@f-gC_3N_4 (Fig. S13†). The dominant component of the pristine 1Fe@f-gC_3N_4 was the g-C_3N_4 phase, as confirmed by the C 1s and N 1s spectra. In the C 1s region, photoelectron emission, typical of sp^2-bonded C atoms in N–C=N, was observed at 288.1 eV, while in the N 1s region three peaks at 398.6 eV (sp^2-hybridized N atoms in C–N=C species), 400.1 eV (©dging N atoms N-$(C)_3$ species) and 401.2 eV (N atoms in amino groups) were found.[82,83] Fe^{n+} species also appeared on the surface of f-gC_3N_4. Due to the low content of this component, it was difficult to determine the chemical state of Fe unequivocally. Nevertheless, the Fe $2p_{3/2}$ peak position at 710.6 eV with an apparent multiplet splitting and a low satellite at *ca.* 718 eV indicated the presence of high-spin Fe^{3+} species. Another evidence confirming this supposition was the orbital splitting of Fe $2p_{3/2}$ and Fe $2p_{1/2}$ of 13.8 eV, which was similar to that reported previously in the literature for Fe^{3+}.[84] The elemental composition of the photocatalyst surface did not change during the process, and the used sample exhibited the same peaks in the individual XPS spectra. However, their intensity decreased due to the deposition of an additional component on the surface. Its nature was revealed by the XPS C 1s spectrum, where two new peaks were distinguished at binding energies of 284.8 eV and 285.9 eV, respectively. The former was typical for C–C/C=C, while the latter was for the oxidized C forms, most likely C–O or C=O.[85]

To obtain better insights into the mechanism of the reaction, the optical properties of the photocatalysts were characterized. Through UV/vis spectroscopy (Fig. S4a†), an absorption edge at 465 nm was observed in the case of gC_3N_4, whereas f-gC_3N_4, 0.5Fe@gC_3N_4 and 0.5Fe@f-gC_3N_4 exhibited a redshift of 30 nm, 34 nm and 34 nm, respectively (corresponding to 0.16 eV, 0.18 ev and 0.18 ev respectively). However, different Fe-loading had a negligible effect on the optical spectrum. The broad and intense absorption peak of the Fe-loaded f-gC_3N_4 catalyst in the visible region inferred that the catalyst could absorb more photons, which was a consequent enhancement of the photocatalytic activity.[86] The difference in the absorption band between gC_3N_4 and Fe-loaded f-gC_3N_4 could be due to the electrostatic interaction between Fe^{+n} and f-gC_3N_4, which promoted the electron delocalization throughout the heptazine framework by Fe^{+n}.[87] This was also evident from EPR spectroscopy, which showed a broadening of the 1Fe@f-gC_3N_4 signal (compared to f-gC_3N_4 one), due to the mutual interaction between the paramagnetic species (Fig. S14†).

The photocatalysts' steady-state photoluminescence (PL) spectra (Fig. S17a†) revealed emission maxima of gC_3N_4 at 471 nm and of Fe-gC_3N_4 at 466 nm. The emission spectra of f-gC_3N_4 and Fe-loaded f-gC_3N_4 were broad and centered around 513 nm. To investigate the charge carrier generation and dynamics, we measured the PL decays of the photocatalysts at their respective emission wavelength (Fig. S17b and c†). The PL decay profiles of all samples were recorded by time-correlated photon counting (TCSPC) spectroscopy and fitted using a tri-

exponential decay equation. The average PL lifetimes and the fitting parameters are given in Table S3†. According to the lifetime fitting parameters, f-gC_3N_4 and Fe-loaded f-gC_3N_4 had longer τ_1 and τ_2 values compared to the gC_3N_4 and Fe-gC_3N_4 catalysts. Additionally, upon increasing Fe-loading in f-gC_3N_4, the carrier lifetimes exhibited an increasing trend of all τ_1, τ_2, and τ_3 values. Although there is a slight difference in the average lifetime of the photocatalysts, the iron loading in f-gC_3N_4 increases the average lifetime, resulting in enhanced photocatalytic activity. This result supported the above-explained enhanced photocatalytic reactivity upon increasing the iron wt% due to a more efficient transfer of photogenerated electrons from f-gC_3N_4 to Fe^{+n}. Following the increase of the charge carrier lifetimes, the generated electrons were available for a longer time for the photocatalysis reaction to efficiently take place. Specifically, in 1Fe@f-gC_3N_4, the τ_3 value, reflecting the lifetime of the free charge carriers that can diffuse over longer distances, has significantly increased.

In addition, to investigate the separation efficiency of photogenerated electron–hole pairs, we recorded the photocatalyst's transient photocurrent responses under the irradiation of a Kessil lamp ($\lambda = 427$ nm). Among all of them, 1Fe@f-gC_3N_4 exhibited the quickest and highest photocurrent which remained stable up to 5 cycles which indicated a more efficient charge separation and faster electron transfer rate to trigger a superior photocatalytic reactivity of the catalyst (Fig.-S18b†). Furthermore, *in situ* EPR spectroscopy showed that the relative number of the photoexcited electrons of f-gC_3N_4 was higher than 1Fe@f-gC_3N_4 due to the facile electron transfer to Fe (Fig. S14†). Additionally, Electrochemical Impedance Spectroscopy (EIS) of gC_3N_4, f-gC_3N_4 and all the Fe-loaded gC_3N_4 and f-gC_3N_4 exhibited decreasing charge transfer resistance, demonstrating the presence of covalent linking in 1Fe@f-gC_3N_4 which significantly enhanced the conductivity (Fig. S18a†). The CO_2 reduction was confirmed by a spin-trapping experiment with DMPO (Fig. S16†). The holes in the valence band were quenched by the sacrificial reductant (TEA) and decreased the electron–hole recombination, as it is evident from the *in situ* EPR investigations (Fig. S15†). In the valence band, TEA reacted with holes and subsequently formed the α-amino radical and protons.[88]

Further to gather detailed information about the reaction mechanism, computational calculations were done (see in the ESI†) and after ≈50 ps of RMD, the sampled structures showed that the adsorption tendency of CO_2 on the metal centers was mainly due to the coordination of one of its oxygens (Fe–O distance about 2.1 Å),[89] and no reaction mechanisms were observed in those conditions. Indeed, the conversion started from an activated adsorption configuration where the carbon atom was connected to the metal center, and the CO_2 molecule adopted a bent arrangement ($CO_2^{\bullet-}$).[90–92] Experimentally, this activation was obtained by light irradiation ($\lambda = 427$ nm), which induced a charge transfer from the catalyst to the molecule, CO_2 chemisorption with the elongation of the C–O bond, bending of O–C–O angle, and finally, dissociation of CO_2 on the catalyst surface into CO and O species.[93,94]

We could mimic this process by including, in the RMD simulations, an electric field in the plane of the melem units (x direction, -0.01 V Å^{-1}). The effect of the external electric field is a perturbation of the atomic charges of the system and, thus, a distortion of the molecular charge distribution. The evolution of the dipole moments imitated a charge transfer from the metal center to the adsorbed CO_2. This is apparent in the atomic charge distribution plots of Fig. S21,† where it is evident the charge transfer from Fe to CO_2 during the first 7.5 ps of the simulation (Fig. S21† – bottom) and the change of nature of the C atom when CO_2 reduces to CO (Fig. S21† – middle plot). The adsorbed CO_2 in a bent geometry was negatively charged. Indeed, from the beginning of the polarized dynamics, CO_2 changed from an extended to a bent conformation and remained adsorbed on the Fe atom through its carbon (Fig. S20†). The stabilized complex received a proton from the solution and formed the adsorbed *COOH species. This species was short-lived, and the OH was quickly released in solution and then protonated. In contrast, CO remained stably adsorbed on the metal center (Fig. S22†). Besides reproducing possible hydrogen exchanges between the solvent and the region around the COO–Fe complex, the mechanisms produced a water molecule that freely migrated in the solution, whereas CO remained connected to the metal.

To refine this picture, we extracted the MD snapshots describing the primary steps of the reaction mechanism, size-reduced them to three melem units with a chelated Fe atom and an adsorbed CO_2 molecule (high-coordination site) or two melem units with a chelated Fe-atom, the f-substituent, and an adsorbed CO_2 molecule (low-coordination site), and carried out density functional theory (DFT) calculations with Gaussian16.[95] These were used to estimate minimum energy structures, charge analyses, possible reaction paths, and relative energy barriers (Fig. 5, 6 and S23†). We optimized the geometries in ACN through the integral equation formalism variant (IEFPCM) of the Polarizable Continuum Model (PCM), using the B3LYP-D3(BJ) functional with the Grimme D3 correction (Becke–Johnson parameters[97]), to account for the van der Waals interactions, and the 6-31(d,p) basis set for all the elements except Fe, which was described with the def2-TZVP basis set.[98] Charge analysis was performed using NBO (full Natural Bond Orbital).[99,100]

Both high- and low-coordination sites provide a similar qualitative picture of the reaction mechanism, in agreement with the results of RMD simulations. In the absence of external stimuli, CO_2^* molecule interacted weakly *via* one of its oxygens with the catalyst metal center (Fe–O equilibrium distance is 2.04 Å, in fair agreement with the results of RMD), which acted as a Lewis acceptor (see state 1 in Fig. 5), as confirmed by the small positive charge carried by CO_2 (about +0.2e) and the charge decrease on Fe after adsorption (about 1.1e, to be compared with 1.3e of a naked Fe atom – Fig. S23†). The CO_2^* activation happened after the addition of a H^+/e^- couple promoted by UV irradiation: a similar bent adsorption configuration obtained by RMD (and shown in state 2 of Fig. S23†) was stabilized by a flow of negative charge to both the CO_2 molecule (charge of ≈ −0.4e) and the Fe center (charge decrease from ≈+1.0e to ≈+0.7e). The

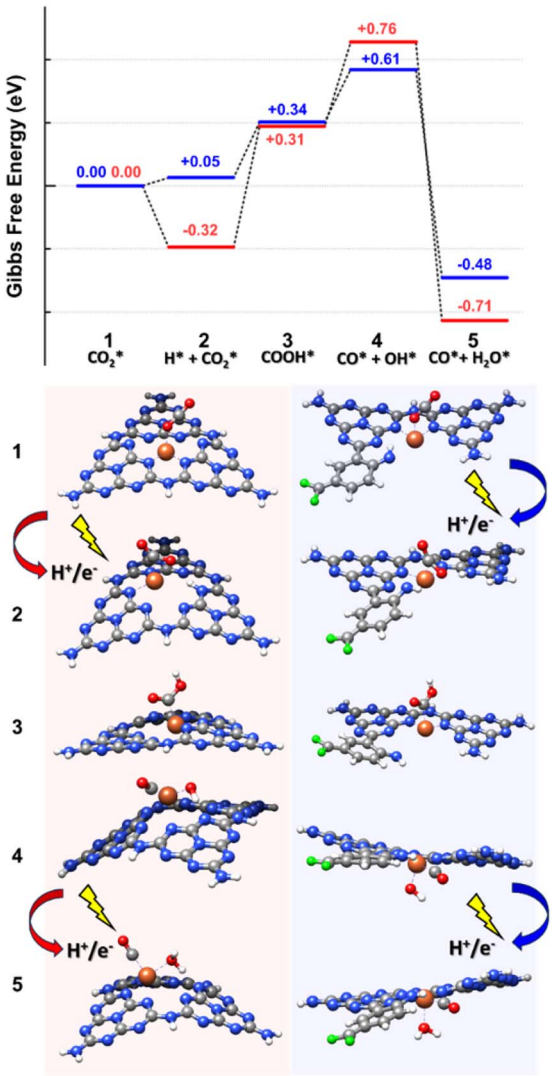

Fig. 5 Reaction mechanism showing CO_2 reduction to CO involving Fe atom in a high-coordination (red path) and a low-coordination (blue path) sites. State 1 is chosen as a reference for energy estimation, whereas the free energies of the other states (from 2 to 5) are estimated at the DFT level by employing the Norskov model.[96] Color code: C gray, N blue, F green, Fe orange, O red, H white.

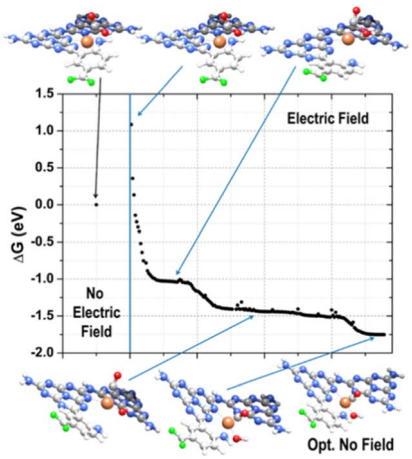

Fig. 6 Reaction path of the adsorbed CO_2 reduction to CO. The DFT minimum energy structures (initial and final points – top left and bottom right ball and stick models) are shown together with the intermediate species indicated by the blue arrows. Color code: C gray, N blue, F green, Fe orange, O red, H white.

proton (as in RMDs) was adsorbed on a nitrogen atom at the edge of a neighboring melem unit. CO_2 negative charging is also evident in the PDOS shown in Fig. S24.†

After proton migration to CO_2^* we obtained the COOH* configuration shown in state 3 (Fig. 5). This positive charge flow allows negative charge back-migration from Fe to the adsorbate (with COOH almost neutral), as shown in Fig. S23.† The elongation and weakening of the bond between the carbon and the hydroxyl group (induced by the catalyst-adsorbate charge transfer, populating the p* LUMO of CO_2 (ref. 88)) can be exasperated until the breaking of the C–O bond realized the configuration shown in state 4 (Fig. 5), which presents CO and OH separately adsorbed on the Fe atom. The positive charge carried by CO was compensated by a reduced charge on Fe (relative to state 2), and the negative charge carried by OH* (about $-0.2e$). States 3 and 4 are at higher energy relative to state 2 ($\approx$1.08 eV for the high-coordination site and 0.56 eV for the low-coordination). The reduced energy difference characterizing the low-coordination site suggests that this can promote CO_2 reduction easier than the high-coordination site and will be further investigated in the following. The UV-vis spectra simulated for state 2 of the low-coordination site, calculated at the TD-DFT level (Fig. S25†), show a dominant peak at about 465 nm, corresponding to a charge transfer from the metal ion to the adsorbed CO_2^* molecule, aiding the C–O bond breaking in overcoming the observed energy difference between states 2 and 4. This agrees with the experimental choice of a blue LED (λ = 427 nm) as the excitation source.

Further addition of a H^+/e^- couple (promoted by UV excitation) led to the configuration of state 5 (Fig. 5), which corresponded to adsorbed CO and H_2O on the Fe catalyst. H_2O carried a slight positive charge (about $+0.2e$), and CO kept its positive charge of about $+0.4e$. The relatively strong dipole between Fe and CO is a clear signal of a strong CO anchoring to the catalytic site, which can be disrupted if the charge flows from Fe to CO. The Gibbs free energy of this last state is lower than that of any other state investigated, confirming the thermodynamic tendency of this system to promote CO_2 reduction. This sequence of events is the same as observed in RMD. We resorted to the electric field option already used for the RMD to recreate a possible dynamics mechanism at the DFT level instead of performing computationally expensive excited-state quantum chemistry simulations. Starting from the optimized complex of the low-coordination corresponding to state 2 (Fig. 5), where the CO_2 molecule was adsorbed with the carbon atom on the metal ion, we emulated the first few steps of the reduction mechanism by applying an external electric field in the -x direction with a magnitude of 0.008 au.

From the examination of the free energy difference plot, it is evident that a low activation energy of $\approx$1.1 eV was necessary to

start the process; this activation energy is reasonable when compared to the energy difference of ≈0.6 eV between states 2 and 4, estimated at the static level (Fig. 6). Then, the mechanism proceeded barrierlessly, passing through two intermediate metastable geometries (plateau regions). The first one is characterized by the appearance of the adsorbed COOH* species (state 3 in Fig. 5), whereas in the second one, the OH detached from C and became connected to the metal center (at a C–Fe–OH angle of about 103°, state 4 in Fig. 5), forming a bond with Fe (with an average Fe–O length of approximately 1.8 Å) and a hydrogen bond with the nitrogen atom of the nearby triazine ring (with an average OH–N distance of roughly 1.8 Å and a donor-H-acceptor angle of about 140°). In the final stable configuration, the hydrogen bond was lost, and the OH group moved to a farther N–O separation of about 3 Å but remained connected to the metal center. Interestingly, when simulated under the effect of the electric field, the energies of states 3 and 4 become lower than that of state 2, indicating a stabilizing effect played by the external perturbation on configurations which, when analyzed in their ground state, resulted instead higher in energy.

Conclusions

In conclusion, we have successfully demonstrated that coupling amorphous FeOOH with f-gC_3N_4 exhibited an efficient visible-light-mediated CO_2 conversion into CO. The presence of FeOOH in functionalized gC_3N_4 modulated the electronic interaction between Fe species and semiconductor, making an efficient photocatalyst for CO_2 reduction. This FeOOH/f-gC_3N_4 composite heterogeneous photocatalyst has shown the highest CO evolution rate (so far reported among Fe-based heterogeneous photocatalysts) of 304 μmol g^{-1} h^{-1} with an excellent selectivity of >99%. This earth-abundant and low-cost photocatalyst also exhibited excellent reactivity and stability for reducing car exhaust gas, which clearly depicted the strong application potential of this chemistry. We strongly believe that our photocatalytic system will open a new strategy in the field of photocatalytic CO_2 reduction.

Author contributions

T. G., P. R. and S. D. conceptualized the project. S. D. supervised the project. T. G and P. R. synthesized the catalysts, conducted the catalytic experiments and the related data processing, and performed materials characterization and analysis with the help of P. F., A. J., A. R., P. K., L. C. and E. D. Furthermore, A. J. collected solid-state NMR spectra and J. R. performed EPR investigations. M. T. and S. B. conducted high-resolution, high angle annular dark-field transmission electron microscope (HAADF-STEM) spectroscopy. G. B. and S. M. performed the theoretical studies. J. S.-A., A. S. and L. S. performed X-ray absorption near edge structure (XANES) and extended X-ray absorption fine structure (EXAFS) measurement and analysis. A. C and E. D performed the steady state spectroscopy. A. R and P. K performed the X-ray photoelectron spectroscopy (XPS). The manuscript was written through the contributions of all authors.

Conflicts of interest

There are no conflicts to declare.

Acknowledgements

S. D. thanks the Francqui start up grant from the University of Antwerp, Belgium for the financial support. T. G. thanks MSCA BOF postdoctoral fellowship. P. R. thanks CSC. E. D. would like to thank the KU Leuven Research Fund for financial support through STG/21/010. J. S. A. acknowledges financial support from MCIN/AEI/10.13039/501100011033 and EU "NextGeneration/PRTR (Project PCI2020-111968/3D-Photocat) and Diamond Synchrotron (Rapid access proposal SP32609). XPS measurements were carried out with the equipment purchased thanks to the financial support of the European Regional Development Fund in the framework of the Polish Innovation Economy Operational Program (contract no. POIG.02.01.00-12-023/08). The research has been supported by a grant from the Faculty of Chemistry under the Strategic Programme Excellence Initiative at Jagiellonian University.

Notes and references

1 I. Bauer and H. J. Knolker, Iron catalysis in organic synthesis, *Chem. Rev.*, 2015, **115**, 3170–3387.
2 V. G. Chandrashekhar, T. Senthamarai, R. G. Kadam, O. Malina, J. Kašlík, R. Zbořil, M. B. Gawande, R. V. Jagadeesh and M. Beller, Silica-supported Fe/Fe–O nanoparticles for the catalytic hydrogenation of nitriles to amines in the presence of aluminium additives, *Nat. Catal.*, 2021, **5**, 20–29.
3 B. Singh, M. B. Gawande, A. D. Kute, R. S. Varma, P. Fornasiero, P. McNeice, R. V. Jagadeesh, M. Beller and R. Zboril, Single-Atom (Iron-Based) Catalysts: Synthesis and Applications, *Chem. Rev.*, 2021, **121**, 13620–13697.
4 A. Furstner, Iron Catalysis in Organic Synthesis: A Critical Assessment of What It Takes To Make This Base Metal a Multitasking Champion, *ACS Cent. Sci.*, 2016, **2**, 778–789.
5 M. Neumeier, U. Chakraborty, D. Schaarschmidt, V. de la Pena O'Shea, R. Perez-Ruiz and A. Jacobi von Wangelin, Combined Photoredox and Iron Catalysis for the Cyclotrimerization of Alkynes, *Angew Chem. Int. Ed. Engl.*, 2020, **59**, 13473–13478.
6 H. T. Zhang, X. J. Su, F. Xie, R. Z. Liao and M. T. Zhang, Iron-Catalyzed Water Oxidation: O-O Bond Formation via Intramolecular Oxo-Oxo Interaction, *Angew Chem. Int. Ed. Engl.*, 2021, **60**, 12467–12474.
7 G. Jin, C. G. Werncke, Y. Escudie, S. Sabo-Etienne and S. Bontemps, Iron-Catalyzed Reduction of CO2 into Methylene: Formation of C-N, C-O, and C-C Bonds, *J. Am. Chem. Soc.*, 2015, **137**, 9563–9566.
8 E. de Smit and B. M. Weckhuysen, The renaissance of iron-based Fischer-Tropsch synthesis: on the multifaceted

catalyst deactivation behaviour, *Chem. Soc. Rev.*, 2008, **37**, 2758–2781.

9 S. Enthaler, K. Junge and M. Beller, Sustainable metal catalysis with iron: from rust to a rising star?, *Angew Chem. Int. Ed. Engl.*, 2008, **47**, 3317–3321.

10 W. Liu, W. Li, A. Spannenberg, K. Junge and M. Beller, Iron-catalysed regioselective hydrogenation of terminal epoxides to alcohols under mild conditions, *Nat. Catal.*, 2019, **2**, 523–528.

11 J. Gu, C. S. Hsu, L. Bai, H. M. Chen and X. Hu, Atomically dispersed Fe(3+) sites catalyze efficient CO2 electroreduction to CO, *Science*, 2019, **364**, 1091–1094.

12 W. Liu, L. Zhang, X. Liu, X. Liu, X. Yang, S. Miao, W. Wang, A. Wang and T. Zhang, Discriminating Catalytically Active FeNx Species of Atomically Dispersed Fe-N-C Catalyst for Selective Oxidation of the C-H Bond, *J. Am. Chem. Soc.*, 2017, **139**, 10790–10798.

13 M. L. Bols, B. E. R. Snyder, H. M. Rhoda, P. Cnudde, G. Fayad, R. A. Schoonheydt, V. Van Speybroeck, E. I. Solomon and B. F. Sels, Coordination and activation of nitrous oxide by iron zeolites, *Nat. Catal.*, 2021, **4**, 332–340.

14 L. Piccirilli, B. Rabell, R. Padilla, A. Riisager, S. Das and M. Nielsen, Versatile CO_2 Hydrogenation-Dehydrogenation Catalysis with a Ru-PNP/Ionic Liquid System, *J. Am. Chem. Soc.*, 2023, **145**, 5655–5663.

15 R. Cauwenbergh, V. Goyal, R. Maiti, K. Natte and S. Das, Challenges and recent advancements in the transformation of CO_2 into carboxylic acids: straightforward assembly with homogeneous 3d metals, *Chem. Soc. Rev.*, 2022, **51**, 9371–9423.

16 P. K. Sahoo, Y. Zhang and S. Das, CO_2-Promoted Reactions: An Emerging Concept for the Synthesis of Fine Chemicals and Pharmaceuticals, *ACS Catal.*, 2021, **11**, 3414–3442.

17 R. Cauwenbergh and S. Das, Photochemical reduction of carbon dioxide to formic acid, *Green Chem.*, 2021, **23**, 2553–2574.

18 Y. Zhang, T. Zhang and S. Das, Catalytic transformation of CO_2 into C1 chemicals using hydrosilanes as a reducing agent, *Green Chem.*, 2020, **22**, 1800–1820.

19 W. Schilling and S. Das, Transition Metal-Free Synthesis of Carbamates Using CO_2 as the Carbon Source, *ChemSusChem*, 2020, **13**, 6246–6258.

20 S. Lin, C. S. Diercks, Y. B. Zhang, N. Kornienko, E. M. Nichols, Y. Zhao, A. R. Paris, D. Kim, P. Yang, O. M. Yaghi and C. J. Chang, Covalent organic frameworks comprising cobalt porphyrins for catalytic CO_2 reduction in water, *Science*, 2015, **349**, 1208–1213.

21 X. Li, Y. Sun, J. Xu, Y. Shao, J. Wu, X. Xu, Y. Pan, H. Ju, J. Zhu and Y. Xie, Selective visible-light-driven photocatalytic CO_2 reduction to CH4 mediated by atomically thin CuIn5S8 layers, *Nat. Energy*, 2019, **4**, 690–699.

22 H. Rao, L. C. Schmidt, J. Bonin and M. Robert, Visible-light-driven methane formation from CO_2 with a molecular iron catalyst, *Nature*, 2017, **548**, 74–77.

23 K. Kosugi, C. Akatsuka, H. Iwami, M. Kondo and S. Masaoka, Iron-Complex-Based Supramolecular Framework Catalyst for Visible-Light-Driven CO_2 Reduction, *J. Am. Chem. Soc.*, 2023, **145**, 10451–10457.

24 Q. Liu, L. Wu, R. Jackstell and M. Beller, Using carbon dioxide as a building block in organic synthesis, *Nat. Commun.*, 2015, **6**, 5933.

25 Q.-W. Song, Z.-H. Zhou and L.-N. He, Efficient, selective and sustainable catalysis of carbon dioxide, *Green Chem.*, 2017, **19**, 3707–3728.

26 C. Vogt, M. Monai, E. B. Sterk, J. Palle, A. E. M. Melcherts, B. Zijlstra, E. Groeneveld, P. H. Berben, J. M. Boereboom, E. J. M. Hensen, F. Meirer, I. A. W. Filot and B. M. Weckhuysen, Understanding carbon dioxide activation and carbon-carbon coupling over nickel, *Nat. Commun.*, 2019, **10**, 5330.

27 S. Kelly and J. A. Sullivan, CO_2 Decomposition in CO_2 and CO_2/H_2 Spark-like Plasma Discharges at Atmospheric Pressure, *ChemSusChem*, 2019, **12**, 3785–3791.

28 Y. Qin, R. Cauwenbergh, S. Pradhan, R. Maiti, P. Frank and S. Das, Straightforward Synthesis of Functionalized γLactams using Impure CO_2 Stream as the Carbon Source, *Nat. Commun.*, 2023, **14**, 7604–7612.

29 Z. Fang, Y. Wang, Y. Hu, B. Yao, Z. Ye and X. Peng, A CO_2-philic ferrocene-based porous organic polymer for solar-driven CO_2 conversion from flue gas, *J. Mater. Chem. A*, 2023, **11**, 18272–18279.

30 Y. Cheng, J. Hou and P. Kang, Integrated Capture and Electroreduction of Flue Gas CO_2 to Formate Using Amine Functionalized SnOx Nanoparticles, *ACS Energy Lett.*, 2021, **6**, 3352–3358.

31 F. Yang, C. Liang, W. Zhou, W. Zhao, P. Li, Z. Hua, H. Yu, S. Chen, S. Deng, J. Li, Y. M. Lam and J. Wang, Oxide-Derived Bismuth as an Efficient Catalyst for Electrochemical Reduction of Flue Gas, *Small*, 2023, **19**, 2300417–2300427.

32 T. Al-Attas, S. K. Nabil, A. S. Zeraati, H. S. Shiran, T. Alkayyali, M. Zargartalebi, T. Tran, N. N. Marei, M. A. Al Bari, H. Lin, S. Roy, P. M. Ajayan, D. Sinton, G. Shimizu and M. G. Kibria, Permselective MOF-Based Gas Diffusion Electrode for Direct Conversion of CO_2 from Quasi Flue Gas, *ACS Energy Lett.*, 2022, **8**, 107–115.

33 S.-H. Guo, X.-J. Qi, H.-M. Zhou, J. Zhou, X.-H. Wang, M. Dong, X. Zhao, C.-Y. Sun, X.-L. Wang and Z.-M. Su, A bimetallic-MOF catalyst for efficient CO_2 photoreduction from simulated flue gas to value-added formate, *J. Mater. Chem. A*, 2020, **8**, 11712–11718.

34 S. Kar, M. Rahaman, V. Andrei, S. Bhattacharjee, S. Roy and E. Reisner, Integrated capture and solar-driven utilization of CO_2 from flue gas and air, *Joule*, 2023, **7**, 1496–1514.

35 M. Dong, J. Zhou, J. Zhong, H. T. Li, C. Y. Sun, Y. D. Han, J. N. Kou, Z. H. Kang, X. L. Wang and Z. M. Su, CO_2 Dominated Bifunctional Catalytic Sites for Efficient Industrial Exhaust Conversion, *Adv. Funct. Mater.*, 2021, **32**, 2110136–2110144.

36 Y. Ma, X. Yi, S. Wang, T. Li, B. Tan, C. Chen, T. Majima, E. R. Waclawik, H. Zhu and J. Wang, Selective photocatalytic CO_2 reduction in aerobic environment by

microporous Pd-porphyrin-based polymers coated hollow TiO_2, *Nat. Commun.*, 2022, **13**, 1400–1409.

37 Z.-Z. Yang, L.-N. He, J. Gao, A.-H. Liu and B. Yu, Carbon dioxide utilization with C–N bond formation: carbon dioxide capture and subsequent conversion, *Energy Environ. Sci.*, 2012, **5**, 6602–6639.

38 Z.-Z. Yang, L.-N. He, Y.-N. Zhao, B. Li and B. Yu, CO2 capture and activation by superbase/polyethylene glycol and its subsequent conversion, *Energy Environ. Sci.*, 2011, **4**, 3971–3975.

39 K. Stanley, S. Kelly and J. A. Sullivan, Effect of Ni NP morphology on catalyst performance in non-thermal plasma-assisted dry reforming of methane, *Appl. Catal., B*, 2023, **328**, 122533–122540.

40 M. Dong, J. X. Gu, C. Y. Sun, X. L. Wang and Z. M. Su, Photocatalytic reduction of low-concentration CO_2 by metal-organic frameworks, *Chem. Commun.*, 2022, **58**, 10114–10126.

41 T. Kajiwara, M. Fujii, M. Tsujimoto, K. Kobayashi, M. Higuchi, K. Tanaka and S. Kitagawa, Photochemical Reduction of Low Concentrations of CO_2 in a Porous Coordination Polymer with a Ruthenium(II)-CO Complex, *Angew Chem. Int. Ed. Engl.*, 2016, **55**, 2697–2700.

42 D. Kim, W. Choi, H. W. Lee, S. Y. Lee, Y. Choi, D. K. Lee, W. Kim, J. Na, U. Lee, Y. J. Hwang and D. H. Won, Electrocatalytic Reduction of Low Concentrations of CO_2 Gas in a Membrane Electrode Assembly Electrolyzer, *ACS Energy Lett.*, 2021, **6**, 3488–3495.

43 H. Kumagai, T. Nishikawa, H. Koizumi, T. Yatsu, G. Sahara, Y. Yamazaki, Y. Tamaki and O. Ishitani, Electrocatalytic reduction of low concentration CO_2, *Chem. Sci.*, 2019, **10**, 1597–1606.

44 T. Nakajima, Y. Tamaki, K. Ueno, E. Kato, T. Nishikawa, K. Ohkubo, Y. Yamazaki, T. Morimoto and O. Ishitani, Photocatalytic Reduction of Low Concentration of CO_2, *J. Am. Chem. Soc.*, 2016, **138**, 13818–13821.

45 X. Wang, K. Maeda, A. Thomas, K. Takanabe, G. Xin, J. M. Carlsson, K. Domen and M. Antonietti, A metal-free polymeric photocatalyst for hydrogen production from water under visible light, *Nat. Mater.*, 2009, **8**, 76–80.

46 Y. Wang, X. Wang and M. Antonietti, Polymeric graphitic carbon nitride as a heterogeneous organocatalyst: from photochemistry to multipurpose catalysis to sustainable chemistry, *Angew Chem. Int. Ed. Engl.*, 2012, **51**, 68–89.

47 P. Ren, T. Zhang, N. Jain, H. Y. V. Ching, A. Jaworski, G. Barcaro, S. Monti, J. Silvestre-Albero, V. Celorrio, L. Chouhan, A. Rokicinska, E. Debroye, P. Kustrowski, S. Van Doorslaer, S. Van Aert, S. Bals and S. Das, An Atomically Dispersed Mn-Photocatalyst for Generating Hydrogen Peroxide from Seawater via the Water Oxidation Reaction (WOR), *J. Am. Chem. Soc.*, 2023, **145**, 16584–16596.

48 X. Wang, K. Maeda, X. Chen, K. Takanabe, K. Domen, Y. Hou, X. Fu and M. Antonietti, Polymer semiconductors for artificial photosynthesis: hydrogen evolution by mesoporous graphitic carbon nitride with visible light, *J. Am. Chem. Soc.*, 2009, **131**, 1680–1681.

49 T. Zhang, W. Schilling, S. U. Khan, H. Y. V. Ching, C. Lu, J. Chen, A. Jaworski, G. Barcaro, S. Monti, K. De Wael, A. Slabon and S. Das, Atomic-Level Understanding for the Enhanced Generation of Hydrogen Peroxide by the Introduction of an Aryl Amino Group in Polymeric Carbon Nitrides, *ACS Catal.*, 2021, **11**, 14087–14101.

50 X. Wang, X. Chen, A. Thomas, X. Fu and M. Antonietti, Metal-Containing Carbon Nitride Compounds: A New Functional Organic-Metal Hybrid Material, *Adv. Mater.*, 2009, **21**, 1609–1612.

51 R. Cheng, H. Jin, M. B. J. Roeffaers, J. Hofkens and E. Debroye, Incorporation of Cesium Lead Halide Perovskites into g-C_3N_4 for Photocatalytic CO_2 Reduction, *ACS Omega*, 2020, **5**, 24495–24503.

52 R. Kuriki, M. Yamamoto, K. Higuchi, Y. Yamamoto, M. Akatsuka, D. Lu, S. Yagi, T. Yoshida, O. Ishitani and K. Maeda, Robust Binding between Carbon Nitride Nanosheets and a Binuclear Ruthenium(II) Complex Enabling Durable, Selective CO_2 Reduction under Visible Light in Aqueous Solution, *Angew Chem. Int. Ed. Engl.*, 2017, **56**, 4867–4871.

53 S. R. E. Reisner, Visible-Light-Driven CO_2 Reduction by Mesoporous Carbon Nitride Modified with Polymeric Cobalt Phthalocyanine, *Angew Chem. Int. Ed. Engl.*, 2019, **58**, 12180–12184.

54 J. Lin, Z. Pan and X. Wang, Photochemical Reduction of CO_2 by Graphitic Carbon Nitride Polymers, *ACS Sustain. Chem. Eng.*, 2014, **2**, 353–358.

55 Y. Zhang, M. Cao, H. Feng, D. Liu and Q. Li, Understanding and Tuning Charge Dynamics in Carbon Nitride/Cobalt(II) Complex Hybrids for Enhanced Photocatalytic CO_2 Reduction, *ACS Catal.*, 2023, **13**, 11376–11388.

56 B. Ma, G. Chen, C. Fave, L. Chen, R. Kuriki, K. Maeda, O. Ishitani, T. C. Lau, J. Bonin and M. Robert, Efficient Visible-Light-Driven CO_2 Reduction by a Cobalt Molecular Catalyst Covalently Linked to Mesoporous Carbon Nitride, *J. Am. Chem. Soc.*, 2020, **142**, 6188–6195.

57 C. Cometto, R. Kuriki, L. Chen, K. Maeda, T. C. Lau, O. Ishitani and M. Robert, A Carbon Nitride/Fe Quaterpyridine Catalytic System for Photostimulated CO_2-to-CO Conversion with Visible Light, *J. Am. Chem. Soc.*, 2018, **140**, 7437–7440.

58 Y. Wei, L. Chen, H. Chen, L. Cai, G. Tan, Y. Qiu, Q. Xiang, G. Chen, T. C. Lau and M. Robert, Highly Efficient Photocatalytic Reduction of CO_2 to CO by In Situ Formation of a Hybrid Catalytic System Based on Molecular Iron Quaterpyridine Covalently Linked to Carbon Nitride, *Angew Chem. Int. Ed. Engl.*, 2022, **61**, e202116832.

59 L. Lin, C. Hou, X. Zhang, Y. Wang, Y. Chen and T. He, Highly efficient visible-light driven photocatalytic reduction of CO_2 over g-C_3N_4 nanosheets/tetra(4-carboxyphenyl)porphyrin iron(III) chloride heterogeneous catalysts, *Appl. Catal., B*, 2018, **221**, 312–319.

60 Z. Jiang, W. Wan, H. Li, S. Yuan, H. Zhao and P. K. Wong, A Hierarchical Z-Scheme alpha-Fe_2O_3/g-C_3N_4 Hybrid for

Enhanced Photocatalytic CO_2 Reduction, *Adv. Mater.*, 2018, **30**, 1706108–1706116.

61 M. Zhang, C. Lai, B. Li, F. Xu, D. Huang, S. Liu, L. Qin, Y. Fu, X. Liu, H. Yi, Y. Zhang, J. He and L. Chen, Unravelling the role of dual quantum dots cocatalyst in 0D/2D heterojunction photocatalyst for promoting photocatalytic organic pollutant degradation, *Chem. Eng. J.*, 2020, **396**, 125343–125355.

62 J. Tang, R. Xu, G. Sui, D. Guo, Z. Zhao, S. Fu, X. Yang, Y. Li and J. Li, Double-Shelled Porous g-C_3N_4 Nanotubes Modified with Amorphous Cu-Doped FeOOH Nanoclusters as 0D/3D Non-Homogeneous Photo-Fenton Catalysts for Effective Removal of Organic Dyes, *Small*, 2023, **19**, e2208232.

63 X. Qian, Y. Wu, M. Kan, M. Fang, D. Yue, J. Zeng and Y. Zhao, FeOOH quantum dots coupled g-C_3N_4 for visible light driving photo- Fenton degradation of organic pollutants, *Appl. Catal., B*, 2018, **237**, 513–520.

64 M. Shi, P. Xiao, J. Lang, C. Yan and X. Yan, Porous g-C_3N_4 and MXene Dual-Confined FeOOH Quantum Dots for Superior Energy Storage in an Ionic Liquid, *Adv. Sci.*, 2020, **7**, 1901975.

65 B. Dong, J. Cui, Y. Gao, Y. Qi, F. Zhang and C. Li, Heterostructure of 1D Ta_3N_5 Nanorod/$BaTaO_2$ N Nanoparticle Fabricated by a One-Step Ammonia Thermal Route for Remarkably Promoted Solar Hydrogen Production, *Adv. Mater.*, 2019, **31**, 1808185–1808191.

66 D. Xiao, K. Dai, Y. Qu, Y. Yin and H. Chen, Hydrothermal synthesis of α-Fe_2O_3/g-C_3N_4 composite and its efficient photocatalytic reduction of Cr(VI) under visible light, *Appl. Surf. Sci.*, 2015, **358**, 181–187.

67 H.-K. Wu, Y.-H. Li, M.-Y. Qi, Q. Lin and Y.-J. Xu, Enhanced photocatalytic CO_2 reduction with suppressing H_2 evolution via Pt cocatalyst and surface SiO_2 coating, *Appl. Catal., B*, 2020, **278**, 119267–119274.

68 D. Tan, J. Zhang, J. Shi, S. Li, B. Zhang, X. Tan, F. Zhang, L. Liu, D. Shao and B. Han, Photocatalytic CO_2 Transformation to CH_4 by Ag/Pd Bimetals Supported on N-Doped TiO_2 Nanosheet, *ACS Appl. Mater. Interfaces*, 2018, **10**, 24516–24522.

69 J. Bonin, M. Robert and M. Routier, Selective and Efficient Photcatalytic CO_2 Reduction to CO Using Visible Light and an Iron Based Homogeneous Catalyst, *J. Am. Chem. Soc.*, 2014, **136**, 16768–16771.

70 P. Huang, J. Huang, S. A. Pantovich, A. D. Carl, T. G. Fenton, C. A. Caputo, R. L. Grimm, A. I. Frenkel and G. Li, Selective CO_2 Reduction Catalyzed by Single Cobalt Sites on Carbon Nitride under Visible-Light Irradiation, *J. Am. Chem. Soc.*, 2018, **140**, 16042–16047.

71 B. Xiong, J. Liu, Y. Yang, Y. Yang and Z. Hua, Effect mechanism of NO on electrocatalytic reduction of CO_2 to CO over Pd@Cu bimetal catalysts, *Fuel*, 2022, **323**, 124339–124345.

72 J. Gao, Y. Wang, S. Zhou, W. Lin and Y. Kong, A Facile One-Step Synthesis of Fe-Doped g-C_3N_4 Nanosheets and Their Improved Visible-Light Photocatalytic Performance, *ChemCatChem*, 2017, **9**, 1708–1715.

73 W. Luo, W. Huang, X. Feng, Y. Huang, X. Song, H. Lin, S. Wang and G. Mailhot, The utilization of Fe-doped g-C_3N_4 in a heterogeneous photo-Fenton-like catalytic system: the effect of different parameters and a system mechanism investigation, *RSC Adv.*, 2020, **10**, 21876–21886.

74 H. Li, C. Shan and B. Pan, Fe(III)-Doped g-C_3N_4 Mediated Peroxymonosulfate Activation for Selective Degradation of Phenolic Compounds via High-Valent Iron-Oxo Species, *Environ. Sci. Technol.*, 2018, **52**, 2197–2205.

75 T. Ma, Q. Shen, B. Z. J. Xue, R. Guan, X. Liu, H. Jia and B. Xu, Facile synthesis of Fe-doped g-C_3N_4 for enhanced visible-light photocatalytic activity, *Inorg. Chem. Commun.*, 2019, **107**, 107451–107459.

76 S. Hu, R. Jin, G. Lu, D. Liu and J. Gui, The properties and photocatalytic performance comparison of Fe^{3+}-doped g-C_3N_4 and Fe_2O_3/g-C_3N_4 composite catalysts, *RSC Adv.*, 2014, **4**, 24863–24869.

77 S. Ye, L. G. Qiu, Y. P. Yuan, Y. J. Zhu, J. Xia and J. F. Zhu, Facile fabrication of magnetically separable graphitic carbon nitride photocatalysts with enhanced photocatalytic activity under visible light, *J. Mater. Chem. A*, 2013, **1**, 3008–3015.

78 Y. Zhang, S. Qin, N. Claes, W. Schilling, P. K. Sahoo, H. Y. V. Ching, A. Jaworski, F. Lemière, A. Slabon, S. Van Doorslaer, S. Bals and S. Das, Direct Solar Energy-Mediated Synthesis of Tertiary Benzylic Alcohols Using a Metal-Free Heterogeneous Photocatalyst, *ACS Sustain. Chem. Eng.*, 2021, **10**, 530–540.

79 H. Fukaya and T. Ono, DFT-GIAO calculations of 19F NMR chemical shifts for perfluoro compounds, *J. Comput. Chem.*, 2004, **25**, 51–60.

80 E. Zhao, W. Zhang, L. Dong, R. Zbořil and Z. Chen, Photocatalytic Transfer Hydrogenation Reactions Using Water as the Proton Source, *ACS Catal.*, 2023, **13**, 7557–7567.

81 A. Jaworski and N. Hedin, Electron correlation and vibrational effects in predictions of paramagnetic NMR shifts, *Phys. Chem. Chem. Phys.*, 2022, **24**, 15230–15244.

82 Y. Huang, B. Chen, J. Duan, F. Yang, T. Wang, Z. Wang, W. Yang, C. Hu, W. Luo and Y. Huang, Graphitic Carbon Nitride (g-C_3N_4): An Interface Enabler for Solid-State Lithium Metal Batteries, *Angew. Chem.*, 2020, **132**, 3728–3733.

83 F. Dong, Z. Zhao, T. Xiong, Z. Ni, W. Zhang, Y. Sun and W. K. Ho, In situ construction of g-C_3N_4/g-C_3N_4 metal-free heterojunction for enhanced visible-light photocatalysis, *ACS Appl. Mater. Interfaces*, 2013, **5**, 11392–11401.

84 C. P. Rajan, N. Abharana, S. N. Jha, D. Bhattacharyya and T. T. John, Local Structural Studies Through EXAFS and Effect of Fe^{2+}or Fe^{3+} Existence in ZnO Nanoparticles, *J. Phys. Chem. C*, 2021, **125**, 13523–13533.

85 M. C. Biesinger, Accessing the robustness of adventitious carbon for charge referencing (correction) purposes in XPS analysis: Insights from a multi-user facility data review, *Appl. Surf. Sci.*, 2022, **597**, 153681–153691.

86 X. Xi, X. Peng, C. Xiong, D. Shi, J. Zhu, W. Wen, X. Zhang and S. Wang, Iron doped graphitic carbon nitride with

peroxidase like activity for colorimetric detection of sarcosine and hydrogen peroxide, *Mikrochim. Acta*, 2020, **187**, 383–393.

87 X. Ye, Y. Cui and X. Wang, Ferrocene-modified carbon nitride for direct oxidation of benzene to phenol with visible light, *ChemSusChem*, 2014, **7**, 738–742.

88 A. M. Masdeu-Bultó, M. Reguero and C. Claver, Mechanistic Insights of Photocatalytic CO_2 Reduction: Experimental versus Computational Studies, *Eur. J. Inorg. Chem.*, 2022, **2022**, e202100975.

89 K. Homlamai, T. Maihom, S. Choomwattana, M. Sawangphruk and J. Limtrakul, Single-atoms supported (Fe, Co, Ni, Cu) on graphitic carbon nitride for CO_2 adsorption and hydrogenation to formic acid: First-principles insights, *Appl. Surf. Sci.*, 2020, **499**, 143928–143934.

90 S. Osella and W. A. Goddard Iii, CO_2 Reduction to Methane and Ethylene on a Single-Atom Catalyst: A Grand Canonical Quantum Mechanics Study, *J. Am. Chem. Soc.*, 2023, **145**, 21319–21329.

91 S. Fozia, A. Hassan, S. A. Reshi, P. Singh, G. A. Bhat, M. Dixit and M. A. Dar, Boosting CO_2 Activation and Reduction by Engineering the Electronic Structure of Graphitic Carbon Nitride through Transition Metal-Free Single-Atom Functionalization, *J. Phys. Chem. C*, 2023, **127**, 11911–11920.

92 G. Gao, Y. Jiao, E. R. Waclawik and A. Du, Single Atom (Pd/Pt) Supported on Graphitic Carbon Nitride as an Efficient Photocatalyst for Visible-Light Reduction of Carbon Dioxide, *J. Am. Chem. Soc.*, 2016, **138**, 6292–6297.

93 S. Liang, L. Huang, Y. Gao, Q. Wang and B. Liu, Electrochemical Reduction of CO_2 to CO over Transition Metal/N-Doped Carbon Catalysts: The Active Sites and Reaction Mechanism, *Adv. Sci.*, 2021, **8**, e2102886.

94 B. M. Abraham, O. Pique, M. A. Khan, F. Vines, F. Illas and J. K. Singh, Machine Learning-Driven Discovery of Key Descriptors for CO_2 Activation over Two-Dimensional Transition Metal Carbides and Nitrides, *ACS Appl. Mater. Interfaces*, 2023, **15**, 30117–30126.

95 M. J. Frisch, G. W. Trucks, H. B. Schlegel, G. E. Scuseria, M. A. Robb, J. R. Cheeseman, G. Scalmani, V. Barone, G. A. Petersson, H. Nakatsuji, X. Li, M. Caricato, A. V. Marenich, J. Bloino, B. G. Janesko, R. Gom-perts, B. Mennucci, H. P. Hratchian, J. V. Ortiz, A. F. Izmay-lov, J. L. Sonnenberg, D. Williams-Young, F. Ding, F. Lippa-rini, F. Egidi, J. Goings, B. Peng, A. Petrone, T. Henderson, D. Ranasinghe, V. G. Zakrzewski, J. Gao, N. Rega, G. Zheng, W. Liang, M. Hada, M. Ehara, K. Toyota, R. Fukuda, J. Ha-segawa, M. Ishida, T. Nakajima, Y. Honda, O. Kitao, H. Nakai, T. Vreven, K. Throssell, J. A. Montgomery Jr, J. E. Peralta, F. Ogliaro, M. J. Bearpark, J. J. Heyd, E. N. Brothers, K. N. Kudin, V. N. Staroverov, T. A. Keith, R. Kobayashi, J. Normand, K. Raghavachari, A. P. Rendell, J. C. Burant, S. S. Iyengar, J. Tomasi, M. Cossi, J. M. Millam, M. Klene, C. Ada-mo, R. Cammi, J. W. Ochterski, R. L. Martin, K. Morokuma, O. Farkas, J. B. Foresman, and D. J. Fox, *Gaussian 16, Revision C.01*, Gaussian, Inc., Wallingford CT, 2016.

96 J. K. Norskov, J. Rossmeisl, A. Logadottir, L. Lindqvist, J. R. Kitchin, T. Bligaard and H. Jónsson, Origin of the overpotential for oxygen reduction at a fuel-cell cathode, *J. Phys. Chem. B*, 2004, **108**, 17886–17892.

97 S. Grimme, S. Ehrlich and L. Goerigk, Effect of the damping function in dispersion corrected density functional theory, *J. Comput. Chem.*, 2011, **32**, 1456–1465.

98 C. A. Ohlin, Energetics of paramagnetic oxide clusters: the Fe(iii) oxyhydroxy Keggin ion, *Phys. Chem. Chem. Phys.*, 2020, **22**, 4043–4050.

99 J. P. Foster and F. Weinhold, Natural Hybrid Orbitals, *J. Am. Chem. Soc.*, 1980, **102**, 7211–7218.

100 A. E. Reed, R. B. Weinstock and F. Weinhold, Natural population analysis, *J. Chem. Phys.*, 1985, **83**, 735–746.